

Effects of X-rays on Perovskite Solar Cells

Michael E. Stuckelberger,* Tara Nietzold, Bradley M. West, Yanqi Luo, Xueying Li, Jérémie Werner, Björn Niesen, Christophe Ballif, Volker Rose, David P. Fenning, and Mariana I. Bertoni

Cite This: *J. Phys. Chem. C* 2020, 124, 17949–17956

Read Online

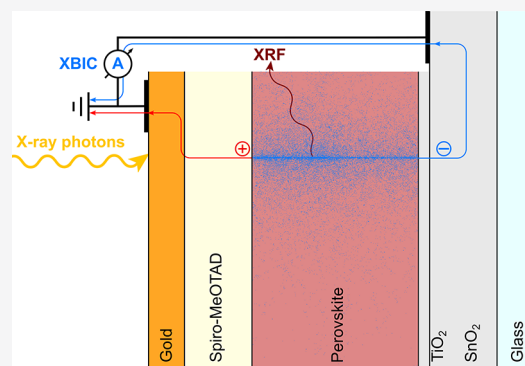
ACCESS |

Metrics & More

Article Recommendations

Supporting Information

ABSTRACT: Synchrotron micro- and nanoprobe beamlines have demonstrated great potential to advance photovoltaic devices. Most importantly, their small X-ray spot size has enabled the direct correlation of electrical performance with elemental composition at subgrain resolution for a variety of polycrystalline solar cells. Whereas the bulk of most inorganic semiconductors is stable under the high X-ray flux of focused X-ray beams, semiconductors with organic components are prone to a variety of degradation mechanisms. This is particularly critical to evaluate for the emerging organometal halide perovskite solar cells. Here, we investigate the effects of hard X-rays on the nanoscale performance and elemental distribution of these solar cells. We show that their composition does not change during common operando and in situ measurements at synchrotron nanoprobe. However, we found a significant X-ray-induced electronic degradation of solar cells with methylammonium lead iodide absorbers. Time- and dose-dependent measurements unveiled two characteristic degradation time constants on the order of 12 and 200 s that are independent of the X-ray flux. On the basis of heat and dose simulations, we attribute the fast decay to the dose-driven creation of recombination centers, while the slow decay is compatible with the observation of compositional changes. Finally, we detail how degradation-induced measurement artifacts can be outrun and showcase the high correlation of the X-ray-beam-induced current with the iodine and lead distribution.



INTRODUCTION

The advent of correlative X-ray microscopy¹ in photovoltaic research is largely based on the codevelopment of brilliant hard-X-ray synchrotron micro- and nanoprobe beamlines at third-generation synchrotrons and of experimental techniques such as X-ray-beam-induced current (XBIC)^{1–4} and voltage (XBIV).^{5–7} These operando measurement techniques are conceptually related to electron- (EBIC) and laser-beam-induced current (LBIC) and give access to the charge collection efficiency in the absorber layer, providing the high penetration depth of LBIC at the high spatial resolution of EBIC. Enabled by the great penetration depth in low-Z materials and by the long working distance, hard X-rays are intrinsically suited to serve as probe beams for in situ measurements of complete solar cell stacks under various conditions.^{6,7}

In the framework of multimodal scanning X-ray microscopy,⁸ the combination of XBIC/XBIV with X-ray fluorescence (XRF) and nanodiffraction measurements has turned out to be particularly powerful for the point-by-point correlation of the electrical performance with the elemental composition and strain in thin-film solar cells with compound polycrystalline absorber layers such as $\text{CuIn}_{1-x}\text{Ga}_x\text{Se}_2$,^{6,9,10} CdTe ,^{11,12} or methylammonium lead iodide (MAPbI₃, $\text{CH}_3\text{NH}_3\text{PbI}_3$).^{13–17}

The record efficiency of perovskite solar cells (PSCs) with an organometal halide absorber has been increasing at an

unprecedented rate, being after a few years of development already beyond the record efficiency of other more established polycrystalline thin-film solar cells.¹⁸ This justifies the tremendous research efforts, although upscaling challenges and degradation have hindered large-scale implementation of PSCs so far. Perovskite solar cells suffer from a variety of degradation mechanisms caused by humidity, light, atmosphere, and combinations thereof.^{19–23} Furthermore, damage of operational PSCs and their absorber layer has been reported from electron and X-ray beams.^{13,24,25} For advanced characterization at the nanoscale—most importantly, to study degradation mechanisms operando and in situ—it is therefore critical to understand and quantify the probe-induced modifications.

METHODS

Solar Cell Fabrication. To study the X-ray-beam-induced damage of PSCs, we have synthesized perovskite solar cells on

Received: May 22, 2020

Revised: July 13, 2020

Published: July 15, 2020



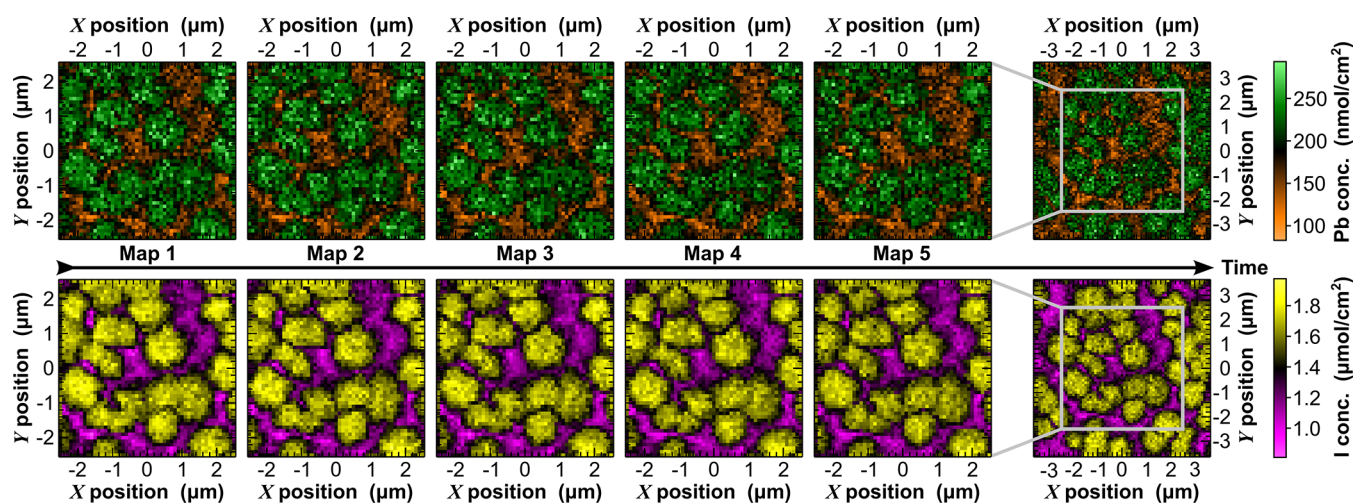


Figure 1. Repeated X-ray fluorescence measurement of a perovskite solar cell area to investigate X-ray-beam-induced changes of the compositional distribution. Top: lead distribution. Bottom: iodine concentration. All maps were taken with $100 \text{ nm} \times 100 \text{ nm}$ pixel size and 1 s dwell time. Reproduced with permission from ref 14. Copyright 2018 Wiley-VCH Verlag GmbH & Co. KGaA.

glass substrates with fluorinated tin oxide (FTO) which serves as front contact during standard solar cell operation. A compact and a mesoporous layer of titanium dioxide was deposited onto the FTO by sputtering and spin-coating, respectively. The archetypal MAPI was spin-coated as an absorber layer on the TiO_2 scaffold following the procedure described elsewhere.²⁶ As hole-transport layer, spiro-MeOTAD was spin-coated on the absorber, and gold was evaporated as back-contact. The solar cell synthesis is detailed elsewhere in greater detail,²⁷ and the sample-specific details are provided in the [Supporting Information](#) (Table S4).

XRF and XBIC Measurements. The experiments were performed at the nanoprobe beamline 26-ID-C²⁸ at Argonne National Laboratory. The angle between the XRF detector and incident X-ray beam is fixed to 90° . The angle between the normal to the sample surface and the incident X-ray beam was 15° , optimized to reduce self-absorption effects in the XRF signal while minimizing the footprint of the X-ray beam. A zone plate focused the coherent X-ray beam at 9 keV to 30–40 nm (FWHM), resulting in a photon flux on the order of 2.6×10^8 photons/s.

The strong X-ray absorption in glass did not allow measuring the XBIC signal with the glass facing the incident X-ray beam, which would correspond to standard solar cell operation. Therefore, the X-ray beam entered the solar cell through the rear contact (p-type) that was grounded to avoid measurement artifacts as discussed elsewhere.¹ The low X-ray absorptance in MAPI leads to a flat charge generation profile throughout the solar cell thickness that is comparable to the illumination with red light and depends only marginally on the illumination side. To reduce the X-ray beam intensity, aluminum filters of 114 and $343 \mu\text{m}$ were used with an X-ray transmittance of 35.3% and 4.4%, respectively. All data shown here are normalized to the X-ray flux assessed by an upstream ion chamber to mitigate artifacts from the decaying electron current in the storage ring.

The careful reader will note that the molar ratio between iodine and lead differs significantly from the nominal stoichiometric ratio of 3 that is expected for the perovskite crystals. This difference is predominantly caused by measurement artifacts: self-absorption of fluorescence photons, errors of thin-film standard calibration, and limited comparability of

the spectrum fitting for Pb_M and I_L peaks cause an apparently off-stoichiometric ratio between the lead and iodine distributions, in this case an underestimation of lead. For further discussion of these effects on the elemental quantification in thin-film devices such as perovskite solar cells, we refer to the literature.^{7,17,29,30} Note that these errors in the *absolute* quantification of elements cancel out in *relative* evaluation. Consequently, these effects do not affect the outcome of this study, as all conclusions will be drawn from a relative comparison of elemental concentrations as a function of time and space.

Simulations. For the quantification of the dose distribution, we have performed numeric simulations of the X-ray photon/solar-cell interaction using a personalized version of PENCYL that is included in the PENELOPE software package.^{31,32} The dose profiles shown in [Figures S6 and S7](#) have been obtained with 10^8 simulated incident photons. The simulation parameters were the same as the experimental parameters (9 keV incident-photon energy, layer stack with the thicknesses and compositions as detailed in [Table S4](#)), except for the beam diameter and the beam/sample-surface angle that were 0 nm and 90° , respectively.

For the evaluation of the temperature distribution, heat transfer simulations were performed in COMSOL Multiphysics software.³³ To simulate the heat flux coming from the X-ray beam absorbed in the sample, we assumed a line source at the origin of uniform magnitude (in W/m) through the thickness of each layer. The magnitude of the line source in each layer was taken from the absorbed energy per X-ray photon in each layer calculated in the PENELOPE dose simulations at a flux of 2.6×10^8 photons/s per the beamline operating specification. X-ray measurements were taken in a vacuum with the sample integrated atop a thick glass substrate, such that heat transfer from the sample is poor. To establish a worst-case heating scenario, we assumed no heat transfer across the upper or lower boundaries of the sample, meaning that we overestimated the temperature rise in the absorber. Further details about the simulations are given in the [Supporting Information](#).

RESULTS

Effects of X-rays on Absorber Composition. First, we shall investigate the impact of X-ray irradiation on the compositional distribution in the solar cell absorber.⁴ Therefore, we have subsequently measured a solar cell area 5 times as shown in Figure 1 and published elsewhere;¹⁴ a sixth map has been taken slightly larger. Comparing the pristine vs remeasured areas by eye, we barely note X-ray-beam-induced modifications, despite the uncommonly long dwell time of 1 s per pixel. As detailed in the Supporting Information, we conclude that compositional variations of the absorber layer are not relevant within commonly used dwell times.

Effects of X-rays on Charge Collection. Figure 2 illustrates the problem of X-ray-beam-induced electrical

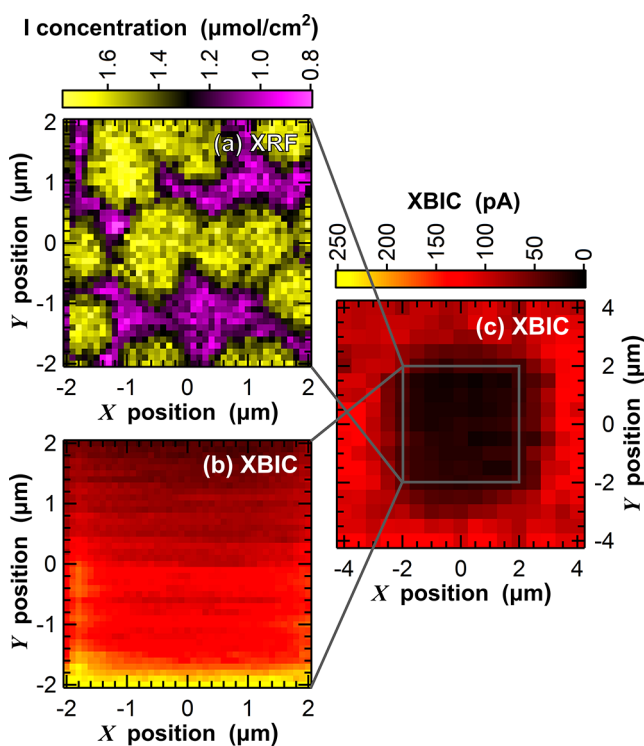


Figure 2. Apparent X-ray-beam-induced degradation of a perovskite solar cell in a synchrotron X-ray nanoprobe. Left: unimpacted iodine distribution from X-ray fluorescence measurements (a) and the degrading X-ray-beam-induced current (XBIC) (b). Measurement started from the left bottom and continued in horizontal lines to the upper right corner. Right: XBIC map of a larger area (c) including the area that was mapped with high resolution. The color scales of both XBIC measurements are equal.

degradation of PSCs with a MAPI absorber when the solar cells are naively measured at X-ray nanoprobe under typical conditions used for other thin-film solar cell measurements (here: 0.5 s dwell time and 100 nm step size). Figure 2a shows the iodine distribution resulting from the XRF measurement, where no degradation is apparent. In contrast, the simultaneously taken XBIC measurement shown in Figure 2b clearly shows a strong signal at the beginning of the scan at coordinates $(X, Y) = (-2 \mu\text{m}, -2 \mu\text{m})$ that decreases to 50% within the first few lines. The strong electronic degradation masks any underlying structure in the XBIC signal. The spatial confinement of the degradation is visible in Figure 2c, for which a quick overview scan was taken with

larger step sizes, outrunning the degradation induced by the second scan.

By comparison of Figure 2c with the $4 \mu\text{m} \times 4 \mu\text{m}$ sized measurement of Figure 2b, we note first that the “electronic crater” is slightly larger than the originally scanned area. Second, we notice that the solar cell performance has decreased even few micrometers away from the “electronic crater”: the XBIC does not reach beyond 50% of the maximum XBIC signal of the pristine sample. Yet, it is noticeable that the X-ray-beam-induced damage is laterally contained. A few dozen micrometers away from the irradiated spot, the solar cell properties are unaffected: the XBIC signal reached values that were comparable to the first XBIC measurements of the pristine solar cell. Furthermore, the open-circuit voltage of the solar cell—evaluated upon illumination of the entire solar cell inside the vacuum chamber by visible light—did not change within the measurement precision.

On one hand, this means that no significant shunts between the two electrodes are created by the X-rays. On the other hand, it indicates that the defects lead to spread-out recombination and act as a sink for the electron–hole pairs that are generated within the diffusion length. Alternative explanations for the apparently spread-out degradation that will be discussed later include beam-induced heating effects and degradation from the tails in the X-ray profile.

For the assessment of the degradation kinetics of the electrical performance, we have measured the XBIC signal during continuous focused irradiation of 3 distinct spots with different X-ray intensities corresponding to 100%, 35.3%, and 4.4% of the maximum focused flux of 2.6×10^8 photons/s. The pristine spots were first illuminated during 11 min—the integrated time of a fast XBIC scan—followed by a minute with shutter closed and another minute with shutter open again. The results are shown in Figure 3. In all three cases, the signal intensity decreased within 11 min to about 50% of the respective initial state as shown in the inset. Note that the degradation kicks in only after a few seconds, which leaves enough time for a quick XBIC measurement before the scan continues to the next pristine spot.

As expected, the XBIC signal decay appears faster at elevated X-ray intensities; quantitative results from the fit with double-exponential functions are given in Table S2. A closer look at the decay rates unveils a fast and slow decay with characteristic decay times that are on the order of 12 and 200 s, respectively. This suggests two distinct degradation mechanisms such as the generation of electronic defects (recombination-active states in the bandgap) followed by the chemical rearrangement (details are provided in the Supporting Information). Note that the fitting unveils similar values of both time constants independent of the flux. However, the low-flux decay shows significantly smaller amplitude of the fast and larger amplitude of the slow component. As a result, the effective decay appears slower at short time scales for the low flux.

For the assessment of the lateral expansion of the degradation effect, we have performed quick XBIC scans across the damaged areas (see Figure 4) in both X and Y directions in the sample surface plane. To reduce the effect of spatial nonuniformities that are responsible for XBIC variations next to the “electronic crater”, the XBIC signal is normalized to the medium XBIC signal of the plateau next to it. In agreement with the previous measurements, we observe a decrease of the XBIC signal to 50% around $(X, Y) = (0, 0)$ where the beam had been parked for a total of 12 min. More remarkable is the

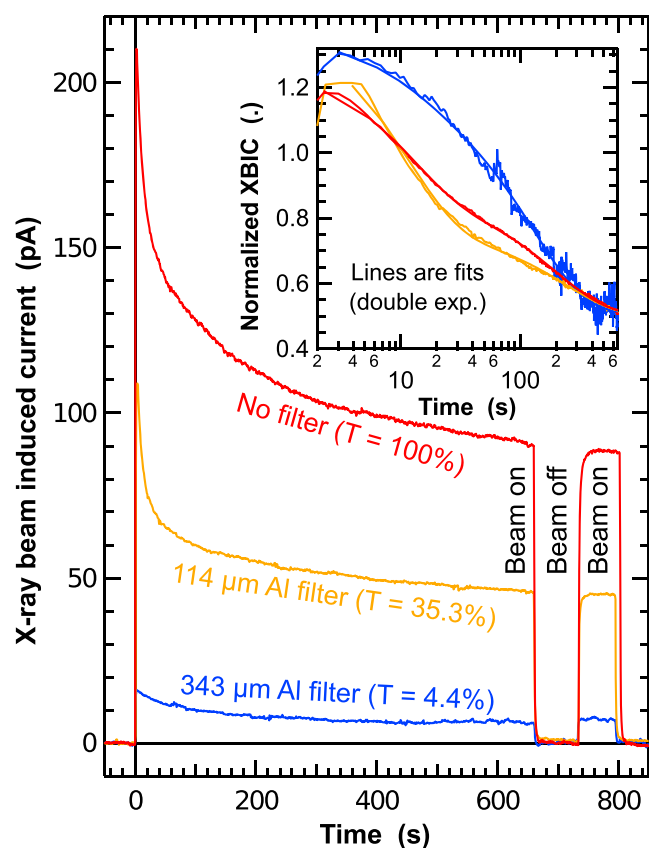


Figure 3. Decay of the XBIC signal at three pristine spots upon irradiation with a focused X-ray beam that was attenuated with Al filters to 100%, 35.3%, and 4.4% of the full incident beam. The inset shows the XBIC signal after normalization to the filter transmittance and fitted to double-exponential functions. The resulting fit parameters are given in Table S2.

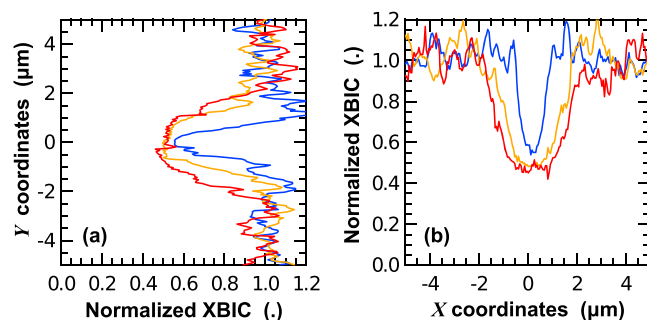


Figure 4. (a) Vertical and (b) horizontal extent of the X-ray-beam-induced damage evaluated by quick XBIC scans across the points irradiated for Figure 3.

lateral dimension of the damage: with increasing irradiation intensity, the diameter of the damaged area increases up to 4 μm , i.e., 2 orders of magnitude larger than the FWHM beam size. Note that the “electronic craters” are considerably larger than the highly localized “compositional craters” that occur upon extended irradiation (details are provided in the Supporting Information, see Figure S4).

Causes for Degradation. We considered four possible causes for the observed X-ray-beam-induced degradation: (1) temperature-induced decomposition from local heating by the X-ray beam, (2) X-ray-beam-induced ablation, (3) compositional changes such as ion diffusion, and (4) dose-related

creation of electronic defect states by the ionizing X-ray irradiation.

(1) We have simulated the X-ray-beam-induced heating in a simplified perovskite solar cell stack as shown in Figure S5. Although we were overestimating the temperature increase by limiting the sample volume and prohibiting heat transfer at boundaries, the simulations indicate no temperature increase beyond a few kelvin, neither at short (10 μs) nor long time scales (100 s). Furthermore, the high thermal conductivity of the sample leads to fast thermal equilibration, which is not compatible with the spatially confined degradation. Therefore, we exclude X-ray-beam-induced temperature increase as the dominant cause of the X-ray-beam-induced decay of the electrical signal.

(2) Cold X-ray-beam-induced ablation can occur in a similar way as laser ablation. Athermal ablation requires pulse duration in the femtosecond range, which is not compatible with the pulses that are about 50 ps long at the synchrotron. Furthermore, ablation is expected to significantly reduce the area density of the ablated material (at least gold as the uppermost material), and the XBIC signal is expected to vanish upon ablation. Neither of these ablation signatures is compatible with the measurements. Therefore, we exclude ablation as the mechanism responsible for the observed XBIC degradation.

(3) As detailed in the Supporting Information, extended exposure to focused X-ray beams leads to a slight reduction of the local concentration of lead and iodine. Overall, the time constants of the elemental-concentration decay are comparable to the slow time constant of the XBIC signal decay, indicating that compositional variations may be responsible for the slow XBIC decay. These results are in agreement with the effects of substoichiometry observed earlier.^{13,14} The larger degradation amplitude and lateral extension length of the XBIC signal can be explained by the large diffusion length of charge carriers in the absorber.

However, the results do not support the hypothesis of compositional variations causing the fast XBIC decay at the time scale of seconds.

(4) For an estimation of the X-ray dose that is absorbed in the perovskite solar cell during XBIC measurements, we have simulated the energy density being deposited by 10^8 photons. We have found that the interaction volume, within which 68% of the dose in the absorber is deposited, spans a diameter of about 200 nm, which gives an idea of the intrinsic limitation of the spatial resolution of such XBIC measurements as detailed elsewhere.^{7,17}

We note that pixels in the beginning of a scan have absorbed significantly less dose prior to the XBIC evaluation there compared to subsequently measured pixels. Figure S7 guides through the process of convoluting the X-ray beam size with the dose distribution from a pencil-like X-ray beam. These simulations are in full agreement with the rapid decrease of the XBIC signal observed experimentally (see Figure 2b) and with the XRF maps that do not suffer from degradation to the same extent. These simulations suggest that the large difference of the interaction radii for XBIC and XRF measurements, being on the order of 100 nm^b and 15 nm, respectively, may further widen the lateral dispersion of XBIC degradation compared to elemental concentration, in addition to the broadening of the XBIC degradation by the charge-carrier diffusion.

These results imply that the electronic degradation may be induced by the deposited dose leading to enhanced

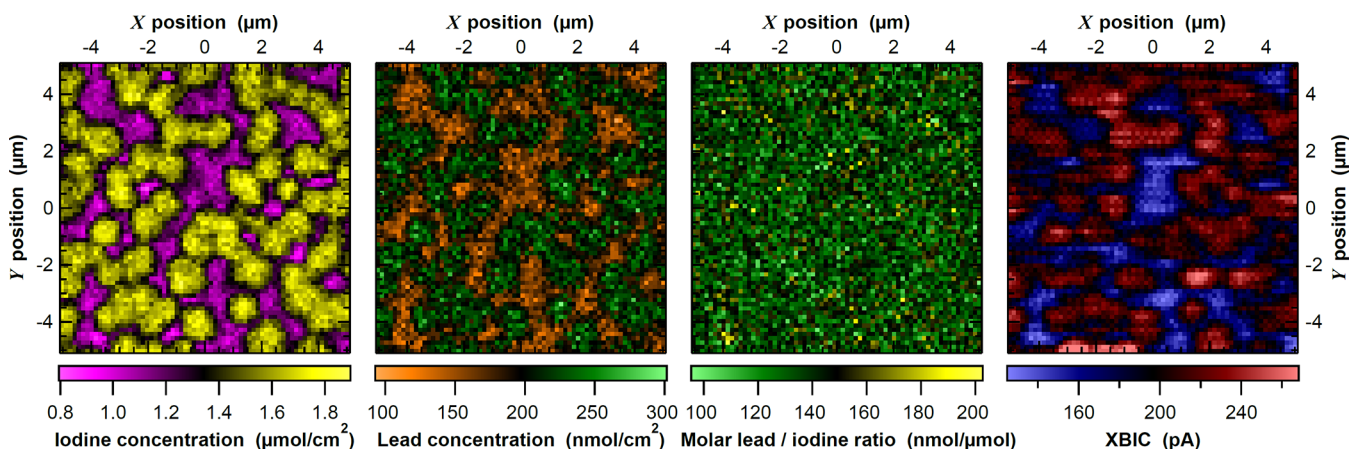


Figure 5. For a comparison of the elemental distribution from XRF measurements with the nanoscale performance from XBIC measurements in the trade-off between signal-to-noise ratio and X-ray-beam-induced degradation, the XBIC measurement was taken first with attenuated X-ray beam (filter transmittance: 35.3%) and short dwell time (0.5 s) followed by an XRF measurement with unattenuated beam and 1 s dwell time.

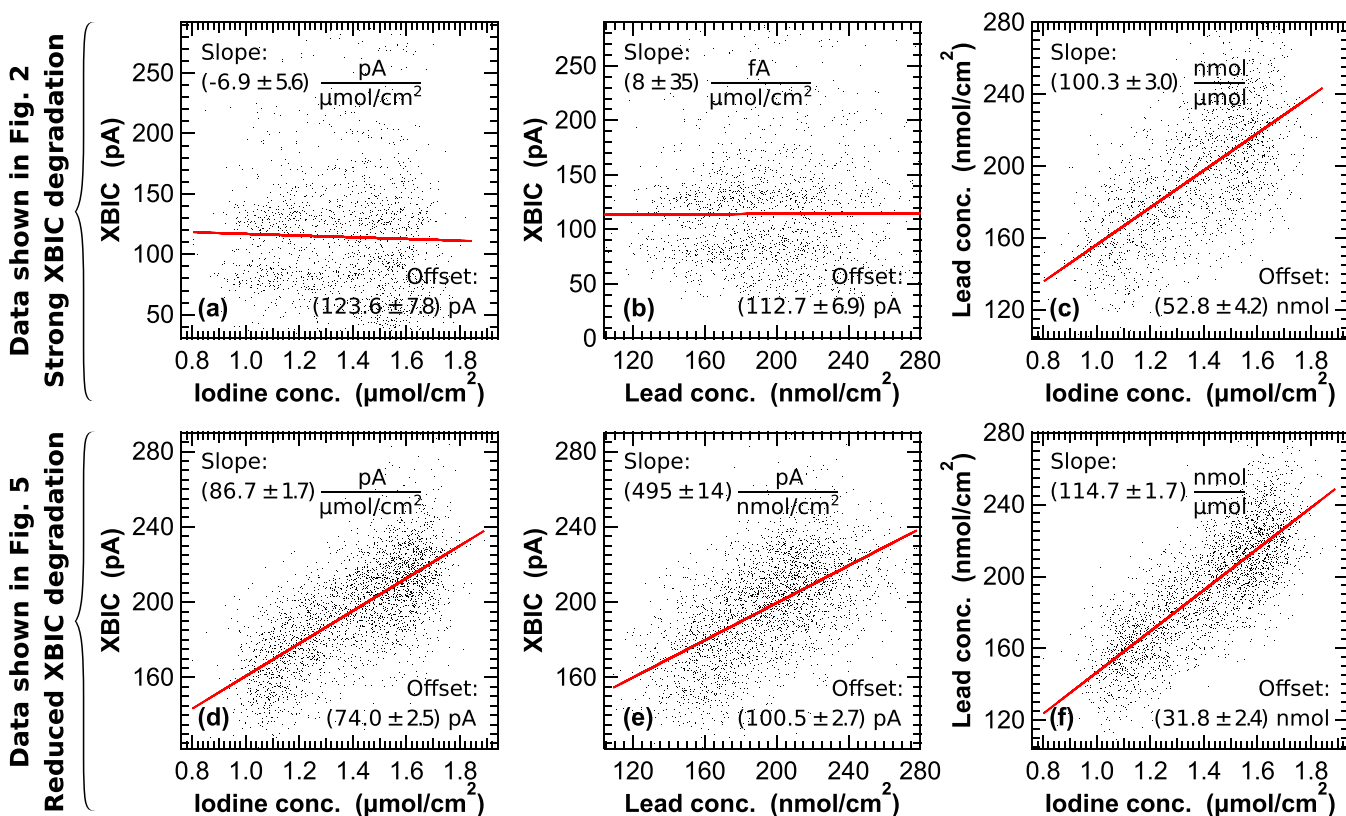


Figure 6. Based on the XBIC and XRF maps shown in Figures 2 and 5, the scatter plots show the correlation between the electrical performance, the lead concentration, and the iodine concentration. Each dot represents one pixel, and the red lines are the result of linear fits. The insets indicate the slope and offset with the standard deviation.

recombination, whereas compositional degradation occurs only locally and at a slower time scale.

Outrunning Degradation Artifacts during XBIC Measurements. Mapping the electrical performance of a degrading sample is often challenging, particularly if the recombination-enhanced area is larger than the beam footprint and step size in combined XBIC/XRF measurements. Nevertheless, there are ways to perform high-quality XBIC/XRF measurements that are hardly affected by the detrimental measurement-induced degradation effects. In the following, we will shortly discuss best-practice approaches that may be

combined for greatest signal-to-noise in both XBIC and XRF measurements.

Optimize Distinct Scans. Combined XBIC/XRF measurements are a special case of multimodal measurements with simultaneous acquisition of different modalities that require a compromise of scan settings that are not compatible for all modalities.⁸ In this case, taking subsequent scans of the same area as shown in our previous work¹³ may lead to the best results: a first scan is optimized for XBIC measurements with short dwell times and attenuated beam to limit beam-induced degradation. A second scan covering the same area can then be

optimized for high sensitivity and spatial resolution of XRF measurements. Because of drift and lack of reproducibility of scan positions that are inevitable at the nanoscale, the XBIC and XRF measurements will require alignment, for example, by image registration.³⁴

Decrease Measurement Time. Given that the signal-to-noise ratio in XBIC measurements is rather limited by currents induced by the environment than by statistics, the integration time can be even below 1 ms if the response chain of the solar cell/amplifier/data acquisition system is fast enough. However, the scanning speed may be limiting, in particular if no continuous “fly scan mode”³⁵ or fast shutter is available, such that the sample degrades during the settling time prior to the measurement at each scan position. In this case, the scan step size may be increased to match the diameter of the interaction volume that ultimately limits the spatial resolution and can be larger than the probe diameter at X-ray nano- and microprobe endstations. This approach has been demonstrated earlier.¹

Use Lock-In Amplification. By use of lock-in amplification, the signal-to-noise ratio of XBIC measurements can be increased by orders of magnitude.^{4,7,36} This allows the X-ray beam to be attenuated without sacrificing the signal-to-noise ratio,^c which leads to a significant reduction of beam damage.

Correlation of XBIC and XRF. Here, we showcase an example of dealing with the trade-off between high-resolution XRF measurements and minimizing electrical degradation during XBIC measurements. First, the XBIC measurement was taken with the nanofocused X-ray beam attenuated to 35.3% and 0.5 s dwell time. The scan speed was limited by the motor settling time of 0.3 s at each scan step. Lacking the fly scan mode and a fast shutter, the high-resolution XBIC scan still suffered from degradation artifacts with the signature of the inverted pattern of Figure S7; these artifacts were corrected as described elsewhere.¹³ While such a correction is clearly not ideal for a quantitative analysis, it still allows to analyze the overall XBIC distribution of degrading samples.

Second, the XRF measurement was taken with an unattenuated beam and 1 s dwell time. The resulting XRF spectra were fitted by using MAPS^{37,38} to extract the molar iodine and lead area concentrations from the I_L and Pb_M lines, respectively. From the iodine and lead distribution, the molar lead-to-iodine ratio was determined. Figure 5 shows the results of these subsequent scans that were optimized for XBIC and XRF measurements, respectively. In contrast to earlier studies, where areas of particularly high lead-to-iodine concentration indicated the presence of a PbI_2 phase that was correlated to low XBIC signal,^{1,13} such features are not clearly visible here, which is typical for a higher quality of the solar cell.

Maps as in Figure 5 lay the foundations for a correlative analysis between electrical performance and elemental distribution as shown in Figure 6. Here, the iodine and lead concentrations are correlated to each other and the XBIC signal, and linear fits were applied to all scatter plots resulting from the point-by-point correlations. This analysis is shown in Figure 6a–c for the measurement with degradation artifacts (data from Figure 2) and in Figure 6d–f for the optimized measurement with fewer degradation artifacts (data from Figure 5).

As expected, Figure 6c,f shows a high correlation between the lead and iodine concentration that were measured simultaneously and are dominated by topological variations. However, the decaying XBIC signal does not correlate with the

elemental distribution, as unveiled by the large uncertainty of the fitted slope in Figure 6a,b.

In contrast, a strong correlation was found between the XBIC signal and the iodine and lead concentrations of the optimized measurements (see Figure 6d,e) as indicated by the small standard deviation of the slope. The clear correlation between XBIC, Pb, and I shows that measurement-induced degradation of the film no longer dominates the XBIC signal, and instead, chemical inferences can be made.

CONCLUSIONS

Our approach correlating the X-ray-beam-induced photocurrent with the elemental distribution at the nanoscale shines light on the relation between performance and composition that is often driven by smallest defects. Although XBIC measurements locally damage perovskite solar cells irreversibly, we have demonstrated ways how to acquire high-quality XBIC data despite the presence of degradation effects. Furthermore, we have quantified the degradation kinetics and run simulations to elucidate the reasons behind. As a result, we could exclude that the degradation is caused by temperature increase. Instead, the results suggest that the degradation of the photocurrent is governed by the dose deposited in the absorber layer across the interaction volume.

This detailed study of experimental parameters for successful measurements of the degradation-sensitive perovskite solar cells will open the door for the in situ and operando characterization of perovskite solar cells. This is of particular interest in view of the nanoprobe endstations at fourth-generation synchrotrons^{39–42} that will enable experiments with 2–3 orders of magnitude higher focused X-ray flux.

There is no doubt that higher flux will lead to more pronounced dose-induced sample degradation. However, on the basis of this study, we may speculate that a dose-independent, slower, degradation component—related for example to diffusion coefficients—could be outrun by fast measurements at a higher dose rate.

Ultimately, such correlative X-ray microscopy experiments will foster the understanding of the relationship between composition and charge collection at the nanoscale and accelerate the development of superior solar cell chemistries and fabrication approaches of perovskite solar cells.

ASSOCIATED CONTENT

Supporting Information

The Supporting Information is available free of charge at <https://pubs.acs.org/doi/10.1021/acs.jpcc.0c04645>.

SI 1: further time-dependent XBIC and XRF measurements to support the kinetics measurements; SI 2: heat transfer simulation; SI 3: simulation of the X-ray interaction volume and the resulting dose upon scanning X-ray microscopy measurements (PDF)

AUTHOR INFORMATION

Corresponding Author

Michael E. Stuckelberger – Photon Science, Deutsches Elektronen-Synchrotron (DESY), 22607 Hamburg, Germany; Ira A. Fulton Schools of Engineering, School of Electrical, Computer and Energy Engineering (ECEE), Defect Lab, Arizona State University (ASU), Tempe, Arizona 85287, United States; orcid.org/0000-0002-8244-5235; Email: michael.stuckelberger@desy.de

Authors

Tara Nietzold – Ira A. Fulton Schools of Engineering, School of Electrical, Computer and Energy Engineering (ECEE), Defect Lab, Arizona State University (ASU), Tempe, Arizona 85287, United States

Bradley M. West – Ira A. Fulton Schools of Engineering, School of Electrical, Computer and Energy Engineering (ECEE), Defect Lab, Arizona State University (ASU), Tempe, Arizona 85287, United States

Yanqi Luo – Department of Nanoengineering, University of California, San Diego, La Jolla, California 92093, United States; orcid.org/0000-0001-5624-9583

Xueying Li – Department of Nanoengineering, University of California, San Diego, La Jolla, California 92093, United States; orcid.org/0000-0001-6185-4446

Jérémie Werner – Institute of Microengineering (IMT), Photovoltaics and Thin Film Electronics Laboratory (PVLAB), Ecole Polytechnique Fédérale de Lausanne (EPFL), 2000 Neuchâtel, Switzerland; orcid.org/0000-0003-4997-9945

Björn Niesen – Institute of Microengineering (IMT), Photovoltaics and Thin Film Electronics Laboratory (PVLAB), Ecole Polytechnique Fédérale de Lausanne (EPFL), 2000 Neuchâtel, Switzerland

Christophe Ballif – Institute of Microengineering (IMT), Photovoltaics and Thin Film Electronics Laboratory (PVLAB), Ecole Polytechnique Fédérale de Lausanne (EPFL), 2000 Neuchâtel, Switzerland

Volker Rose – Advanced Photon Source (APS) and Center for Nanoscale Materials (CNM), Argonne National Laboratory (ANL), Lemont, Illinois 60439, United States

David P. Fenning – Department of Nanoengineering, University of California, San Diego, La Jolla, California 92093, United States; orcid.org/0000-0002-4609-9312

Mariana I. Bertoni – Ira A. Fulton Schools of Engineering, School of Electrical, Computer and Energy Engineering (ECEE), Defect Lab, Arizona State University (ASU), Tempe, Arizona 85287, United States; orcid.org/0000-0002-0415-837X

Complete contact information is available at: <https://pubs.acs.org/10.1021/acs.jpcc.0c04645>

Notes

The authors declare no competing financial interest.

ACKNOWLEDGMENTS

We greatly acknowledge Dr. Martin Holt (ANL) and Geneviève Hall (ASU) for fruitful discussions and Chris Roehrig (ANL) for technical support. We acknowledge funding from the U.S. Department of Energy under Contract DEEE0005848. Use of the Advanced Photon Source, and the Center for Nanoscale Materials, Office of Science user facilities, was supported by the U.S. Department of Energy, Office of Science, Office of Basic Energy Sciences, under Contract DE-AC02-06CH11357. This material is based upon work at UC San Diego supported by the National Science Foundation under Grant DMR-1848371 and the California Energy Commission Advance Breakthrough Award EPC-16-050. The research leading to these results has received funding from Deutsches Elektronen-Synchrotron DESY.

ADDITIONAL NOTES

^aNote that these measurements based on hard X-rays are not sensitive to compositional variations of organic absorber components.

^bThe interaction radius of 100 nm from high-energy secondary photons and electrons is only a lower limit and does not take into account the diffusion length of the charge carriers that may be larger.

^cVarying the beam intensity leads to different charge-injection levels in the solar cell; thus, the charge-collection and recombination mechanisms may change.

REFERENCES

- (1) Stuckelberger, M.; West, B.; Nietzold, T.; Lai, B.; Maser, J. M.; Rose, V.; Bertoni, M. I. Review: Engineering solar cells based on correlative X-ray microscopy. *J. Mater. Res.* **2017**, *32*, 1825–1854.
- (2) Hieslmair, H.; Istratov, A. A.; Sachdeva, R.; Weber, E. R. New synchrotron-radiation based technique to study localized defects in silicon: “EBIC” with X-ray excitation. *10th Workshop on Crystalline Silicon Solar Cell Materials and Processes* **2010**, 162–165.
- (3) Vyvenko, O. F.; Buonassisi, T.; Istratov, A. A.; Hieslmair, H.; Thompson, A. C.; Schindler, R.; Weber, E. R. X-ray beam induced current—a synchrotron radiation based technique for the in situ analysis of recombination properties and chemical nature of metal clusters in silicon. *J. Appl. Phys.* **2002**, *91*, 3614–3617.
- (4) Ossig, C.; Nietzold, T.; West, B. M.; Bertoni, M. I.; Falkenberg, G.; Schroer, C. G.; Stuckelberger, M. E. X-ray beam induced current measurements for multi-modal X-ray microscopy of solar cells. *J. Visualized Exp.* **2019**, e60001.
- (5) Stuckelberger, M.; Nietzold, T.; West, B. M.; Lai, B.; Maser, J.; Rose, V.; Bertoni, M. I. X-Ray beam induced voltage: A novel technique for electrical nanocharacterization of solar cells. *Proc. Photovoltaic Specialist Conference (PVSC)* **2017**, 2179–2184.
- (6) Stuckelberger, M.; Nietzold, T.; West, B. M.; Farshchi, R.; Poplavskyy, D.; Bailey, J.; Lai, B.; Maser, J.; Bertoni, M. I. How does CIGS performance depend on temperature at the microscale? *IEEE Journal of Photovoltaics* **2018**, *8*, 278–287.
- (7) Stuckelberger, M. E.; Nietzold, T.; West, B.; Farshchi, R.; Poplavskyy, D.; Bailey, J.; Lai, B.; Maser, J. M.; Bertoni, M. I. Defect activation and annihilation in CIGS solar cells: an operando x-ray microscopy study. *J. Phys.: Energy* **2020**, *2*, 025001.
- (8) Stuckelberger, M. E. Multimodal scanning X-ray microscopy at nanoprobe endstations of fourth-generation synchrotrons. *Spectroscopy* **2019**, *34*, 42–44.
- (9) West, B.; Stuckelberger, M.; Guthrey, H.; Chen, L.; Lai, B.; Maser, J.; Rose, V.; Shafarman, W.; Al-Jassim, M.; Bertoni, M. I. Grain engineering: How nanoscale inhomogeneities can control charge collection in solar cells. *Nano Energy* **2017**, *32*, 488–493.
- (10) Ulvestad, A.; Hruszkewycz, S. O.; Holt, M. V.; Hill, M. O.; Calvo-Almazán, I.; Maddali, S.; Huang, X.; Yan, H.; Nazaretski, E.; Chu, Y. S.; et al. Multimodal X-ray imaging of grain-level properties and performance in a polycrystalline solar cell. *J. Synchrotron Radiat.* **2019**, *26*, 1316–1321.
- (11) Stuckelberger, M.; West, B.; Husein, S.; Guthrey, H.; Al-Jassim, M.; Chakraborty, R.; Buonassisi, T.; Maser, J. M.; Lai, B.; Stripe, B.; et al. Latest developments in the x-ray based characterization of thin-film solar cells. *Proc. Photovoltaic Specialist Conference (PVSC)* **2015**, 1–6.
- (12) Calvo-Almazán, I.; Ulvestad, A. P.; Colegrove, E.; Ablekim, T.; Holt, M. V.; Hill, M. O.; Maddali, S.; Lauhon, L. J.; Bertoni, M. I.; Huang, X.; et al. Strain Mapping of CdTe Grains in Photovoltaic Devices. *IEEE Journal of Photovoltaics* **2019**, *9*, 1790–1799.
- (13) Stuckelberger, M.; Nietzold, T.; Hall, G. N.; West, B.; Werner, J.; Niesen, B.; Ballif, C.; Rose, V.; Fenning, D. P.; Bertoni, M. I. Charge collection in hybrid perovskite solar cells: relation to the nanoscale elemental distribution. *IEEE Journal of Photovoltaics* **2017**, *7*, 590–597.

- (14) Luo, Y.; Aharon, S.; Stuckelberger, M.; Magana, E.; Lai, B.; Bertoni, M. I.; Etgar, L.; Fenning, D. P. The relationship between chemical flexibility and nanoscale charge collection in hybrid halide perovskites. *Adv. Funct. Mater.* **2018**, *28*, 1706995.
- (15) Li, X.; Luo, Y.; Holt, M. V.; Cai, Z.; Fenning, D. P. Residual nanoscale strain in cesium lead bromide perovskite reduces stability and shifts local luminescence. *Chem. Mater.* **2019**, *31*, 2778–2785.
- (16) Correa-Baena, J.-P.; Luo, Y.; Brenner, T. M.; Snider, J.; Sun, S.; Li, X.; Jensen, M. A.; Hartono, N. T. P.; Nienhaus, L.; Wieghold, S.; et al. Homogenized halides and alkali cation segregation in alloyed organic-inorganic perovskites. *Science* **2019**, *363*, 627–631.
- (17) Kodur, M.; Kumar, R. E.; Luo, Y.; Cakan, D. N.; Li, X.; Stuckelberger, M. E.; Fenning, D. P. X-ray Microscopy of Halide Perovskites: Techniques, Applications, and Prospects. *Adv. Energy Mater.* **2020**, *10*, 1903170.
- (18) Green, M. A.; Dunlop, E. D.; Hohl-Ebinger, J.; Yoshita, M.; Kopidakis, N.; Ho-Baillie, A. W. Solar cell efficiency tables (version 55). *Prog. Photovoltaics* **2020**, *28*, 3–15.
- (19) Leguy, A. M. A.; Hu, Y.; Campoy-Quiles, M.; Alonso, M. I.; Weber, O. J.; Azarhoosh, P.; van Schilfgaarde, M.; Weller, M. T.; Bein, T.; Nelson, J.; Docampo, P.; Barnes, P. R. F. Reversible hydration of $\text{CH}_3\text{NH}_3\text{PbI}_3$ in films, single crystals, and solar cells. *Chem. Mater.* **2015**, *27*, 3397–3407.
- (20) Hall, G. N.; Stuckelberger, M.; Nietzold, T.; Hartman, J.; Park, J.-S.; Werner, J.; Niesen, B.; Cummings, M. L.; Rose, V.; Ballif, C.; et al. The role of water in the reversible optoelectronic degradation of hybrid perovskites at low pressure. *J. Phys. Chem. C* **2017**, *121*, 25659–25665.
- (21) Leijtens, T.; Eperon, G. E.; Noel, N. K.; Habisreutinger, S. N.; Petrozza, A.; Snaith, H. J. Stability of metal halide perovskite solar cells. *Adv. Energy Mater.* **2015**, *5*, 1500963.
- (22) Snaith, H. J.; Hacked, P. Enabling reliability assessments of pre-commercial perovskite photovoltaics with lessons learned from industrial standards. *Nature Energy* **2018**, *3*, 459–465.
- (23) Rong, Y.; Hu, Y.; Mei, A.; Tan, H.; Saidaminov, M. I.; Seok, S. I.; McGehee, M. D.; Sargent, E. H.; Han, H. Challenges for commercializing perovskite solar cells. *Science* **2018**, *361*, eaat8235.
- (24) Yuan, H.; Debroye, E.; Janssen, K.; Naiki, H.; Steuwe, C.; Lu, G.; Moris, M.; Orgiu, E.; Uji-i, H.; De Schryver, F.; et al. Degradation of methylammonium lead iodide perovskite structures through light and electron beam driven ion migration. *J. Phys. Chem. Lett.* **2016**, *7*, 561–566.
- (25) Rothmann, M. U.; Li, W.; Zhu, Y.; Liu, A.; Ku, Z.; Bach, U.; Etheridge, J.; Cheng, Y.-B. Structural and chemical changes to $\text{CH}_3\text{NH}_3\text{PbI}_3$ induced by electron and gallium ion beams. *Adv. Mater.* **2018**, *30*, 1800629.
- (26) Jeon, N. J.; Noh, J. H.; Kim, Y. C.; Yang, W. S.; Ryu, S.; Seok, S. I. Solvent engineering for high-performance inorganicorganic hybrid perovskite solar cells. *Nat. Mater.* **2014**, *13*, 897–903.
- (27) Werner, J.; Dubuis, G.; Walter, A.; Löper, P.; Moon, S.-J.; Nicolay, S.; Morales-Masis, M.; De Wolf, S.; Niesen, B.; Ballif, C. Sputtered rear electrode with broadband transparency for perovskite solar cells. *Solar Energy Mater. Sol. Cells* **2015**, *141*, 407–413.
- (28) Winarski, R. P.; Holt, M. V.; Rose, V.; Fuesz, P.; Carbaugh, D.; Benson, C.; Shu, D.; Kline, D.; Stephenson, G. B.; McNulty, I.; et al. A hard X-ray nanoprobe beamline for nanoscale microscopy. *J. Synchrotron Radiat.* **2012**, *19*, 1056–1060.
- (29) West, B.; Stuckelberger, M.; Jeffries, A.; Gangam, S.; Lai, B.; Stripe, B.; Maser, J.; Rose, V.; Vogt, S.; Bertoni, M. I. X-ray fluorescence at nanoscale resolution for multicomponent layered structures: a solar cell case study. *J. Synchrotron Radiat.* **2017**, *24*, 288–295.
- (30) Ziska, C.; Ossig, C.; Pyrlík, N.; Carron, R.; Avancini, E.; Fevola, G.; Kolditz, A.; Siebels, J.; Kipp, T.; Cai, Z.; Holt, M. V.; Stuckelberger, M. E. Quantifying the elemental distribution in solar cells from X-ray fluorescence measurements with multiple detector modules. *Proc. Photovoltaic Specialist Conference (PVSC)*, 2020.
- (31) Salvat, F.; Fernández-Varea, J. M.; Sempau, J. PENELOPE-2006: A code system for Monte Carlo simulation of electron and photon transport. Workshop Proceedings, 2006.
- (32) Salvat, F.; Fernández-Varea, J. M.; Acosta, E.; Sempau, J. PENELOPE2014, a code system for Monte Carlo simulation of electron and photon transport. Available at: <http://www.oecd-neo.org/tools/abstract/detail/nea-1525> (accessed February 15, 2020).
- (33) COMSOL Multiphysics®. Stockholm, Sweden. Available at: <http://www.comsol.com> (accessed February 15, 2020).
- (34) Pyrlík, N.; Ossig, C.; Ziska, C.; Fevola, G.; Garrevoet, J.; Falkenberg, G.; Schropp, A.; Stuckelberger, M. E. Image registration in multi-modal scanning microscopy: a solar cell case study. Proc. Photovoltaic Specialist Conference (PVSC), 2020.
- (35) Morishige, A. E.; Laine, H. S.; Looney, E. E.; Jensen, M. A.; Vogt, S.; Li, J. B.; Lai, B.; Savin, H.; Buonassisi, T. Increased throughput and sensitivity of synchrotron-based characterization for photovoltaic materials. *IEEE Journal of Photovoltaics* **2017**, *7*, 763–771.
- (36) Stuckelberger, M.; Nietzold, T.; West, B. M.; Walker, T.; Ossig, C.; Wittwer, F.; Deng, J.; Maser, J. M.; Lai, B.; Cai, Z.; et al. Challenges and opportunities with highly brilliant X-ray sources for multi-modal in-situ and operando characterization of solar cells. *Microsc. Microanal.* **2018**, *24* (S2), 434–435.
- (37) Vogt, S. MAPS: A set of software tools for analysis and visualization of 3D X-ray fluorescence data sets. *J. Phys. IV* **2003**, *104*, 635–638.
- (38) Nietzold, T.; West, B. M.; Stuckelberger, M.; Lai, B.; Vogt, S.; Bertoni, M. I. Quantifying X-ray fluorescence data using MAPS. *J. Visualized Exp.* **2018**, *132*, e56042.
- (39) Hettel, R. The Advanced Photon Source Upgrade Plan Approved. *Synchrotron Radiation News* **2019**, *32*, 34–35.
- (40) Schroer, C. G.; Agapov, I.; Brefeld, W.; Brinkmann, R.; Chae, Y.-C.; Chao, H.-C.; Eriksson, M.; Keil, J.; Nuel Gavaldà, X.; Röhlberger, R.; et al. PETRA IV: the ultralow-emittance source project at DESY. *J. Synchrotron Radiat.* **2018**, *25*, 1277–1290.
- (41) Raimondi, P. ESRF–EBS: The Extremely Brilliant Source Project. *Synchrotron Radiation News* **2016**, *29*, 8–14.
- (42) Tavares, P. F.; Al-Dmour, E.; Andersson, Å.; Cullinan, F.; Jensen, B. N.; Olsson, D.; Olsson, D. K.; Sjöström, M.; Tarawneh, H.; Thorin, S.; et al. Commissioning and first-year operational results of the MAX IV 3 GeV ring. *J. Synchrotron Radiat.* **2018**, *25*, 1291–1316.
- (43) Haynes, W. M. *CRC Handbook of Chemistry and Physics*, 2016; <http://hbcponline.com> (last accessed February 15, 2020).
- (44) Onoda-Yamamuro, N.; Matsuo, T.; Suga, H. Calorimetric and IR spectroscopic studies of phase transitions in methylammonium trihalogenoplumbates (II). *J. Phys. Chem. Solids* **1990**, *51*, 1383–1395.
- (45) Guo, Z.; Yoon, S. J.; Manser, J. S.; Kamat, P. V.; Luo, T. Structural Phase- and Degradation-Dependent Thermal Conductivity of $\text{CH}_3\text{NH}_3\text{PbI}_3$ Perovskite Thin Films. *J. Phys. Chem. C* **2016**, *120*, 6394–6401.
- (46) Hata, T.; Giorgi, G.; Yamashita, K. The Effects of the Organic-Inorganic Interactions on the Thermal Transport Properties of $\text{CH}_3\text{NH}_3\text{PbI}_3$. *Nano Lett.* **2016**, *16*, 2749–2753.
- (47) Smith, D. S.; Grandjean, S.; Absi, J.; Kadiebu, S.; Fayette, S. Grain-boundary thermal resistance in polycrystalline oxides: alumina, tin oxide, and magnesia. *High Temp. - High Pressures* **2003**, *35/36*, 93–100.
- (48) Schott, Data sheet AF 32 thin glass; <http://www.schott.com> (last accessed February 15, 2020).
- (49) Solaronix, 2016; <http://www.solaronix.com> (last accessed February 15, 2020).
- (50) Stoumpos, C. C.; Malliakas, C. D.; Kanatzidis, M. G. Semiconducting tin and lead iodide perovskites with organic cations: phase transitions, high mobilities, and near-infrared photoluminescent properties. *Inorg. Chem.* **2013**, *52*, 9019–9038.
- (51) Peuchert, U.; Brix, P. *Alkali-Free Aluminoborosilicate Glasses, and Uses Thereof*, 2007.

Effects of X-Rays on Perovskite Solar Cells

Michael E. Stuckelberger,^{*,†,⊥} Tara Nietzold,[‡] Bradley M. West,[‡] Yanqi Luo,[¶]
Xueying Li,[¶] Jérémie Werner,[§] Björn Niesen,[§] Christophe Ballif,[§] Volker
Rose,^{||,#} David P. Fenning,[¶] and Mariana I. Bertoni[‡]

[†]*Deutsches Elektronen-Synchrotron, Photon Science, Notkestr. 85, 22607 Hamburg, Germany*

[‡]*Arizona State University (ASU), Ira A. Fulton Schools of Engineering, School of Electrical, Computer and Energy Engineering (ECEE), Defect Lab, 551 E. Tylor Mall, Tempe, AZ 85287, United States of America*

[¶]*University of California San Diego, Department of Nanoengineering, La Jolla, CA 92093, United States of America*

[§]*Ecole Polytechnique Fédérale de Lausanne (EPFL), Institute of Microengineering (IMT), Photovoltaics and Thin Film Electronics Laboratory (PVLAB), Rue de la Maladière 71, 2000 Neuchâtel, Switzerland*

^{||}*Argonne National Laboratory (ANL), Advanced Photon Source (APS), 9700 S. Cass Avenue, Lemont, IL 60439, United States of America*

[⊥]*Arizona State University (ASU), Ira A. Fulton Schools of Engineering, School of Electrical, Computer and Energy Engineering (ECEE), Defect Lab, 551 E. Tylor Mall, Tempe, AZ 85287, United States of America*

[#]*Argonne National Laboratory (ANL), Center for Nanoscale Materials (CNM), 9700 S. Cass Avenue, Lemont, IL 60439, United States of America*

E-mail: michael.stuckelberger@desy.de

Contents

SI 1

Further time-dependent XBIC and XRF measurements to support the kinetics measurements

Figure S1: Compositional change during the measurements shown in Fig. 1

Figure S2: Compositional distribution measured with varying dwell times

Figure S3: Overview of the compositional distribution including the areas shown in Fig. S2

Figure S4: Kinetics of compositional change during point-wise irradiation

Table S1: Fit parameters of the iodine and lead kinetics during measurements shown in Fig. S4

Table S2: Fit parameters of the XBIC kinetics during measurements shown in Fig. 3

SI 2

Heat transfer simulation

Table S3: Simplified solar cell structure with parameters for thermal heat transfer simulations

Figure S5: Simulated temperature profile of perovskite solar cell upon X-ray irradiation

SI 3

Simulation of the X-ray interaction volume and the resulting dose upon scanning X-ray microscopy measurements

Table S4: Solar cell structure with parameters for X-ray dose simulations

Figure S6: Simulation of the X-ray dose distribution in a perovskite solar cell

Figure S7: Simulation of the X-ray dose distribution in a perovskite solar cell during scanning

Supp. info. 1

Over the course of all measurements shown in Fig. 1, the statistical analysis seems to unveil a small decrease of the absorber material on the order of 1.5 and 3.4% for iodine and lead, respectively, as shown in Fig. S1(a). The histograms in Fig. S1(b-d) indicate that the decrease is homogeneously distributed between areas with low and high concentrations, and also the titanium signal decreases. Both are indicators that this decrease of the XRF signal is dominated by a drift of the X-ray focusing optics rather than by an effective decrease of the elemental concentrations.

For confirmation, we have measured 4 maps with varying dwell time from 0.5 s up to 5 s per pixel. The resulting maps with the iodine and lead distributions are shown in Fig. S2. As expected, we observe an enhanced signal-to-noise ratio with increasing dwell time.

For the verification of the hypothesis of beam-induced composition changes, we have taken an overview scan including the 4 aforementioned maps as shown in Fig. S3. Only for extraordinarily long dwell times of > 1 s, a lower heavy-ion concentration might be observed, which confirms the result from Fig. 1 and Fig. S1 that compositional changes are uncritical for most XRF scans.

In contrast, we do observe a decrease of the iodine and lead concentrations in the extreme case of extended illumination when the beam is parked on single spots without scanning. As shown in Fig. S4, we have irradiated 4 pristine spots during 14 min with the unattenuated focused beam. Hereby, both iodine and lead concentrations decreased by about 25% except in the spot that contains less absorber material from the beginning. The time constants from fits of the compositional change with exponential functions, τ , are given in Tab. S1. They are compatible with the longer time constants of the electronic change, τ_2 (see Tab. S2), while no fast compositional change corresponding to τ_1 is observed.

The overview map taken after the spot-wise irradiation unveils that the compositional decrease is spatially contained to few hundred

nanometers. Therefore, the compositional decrease is not relevant for standard scanning X-ray microscopy measurements, and the dimensions of the lateral damage are considerably smaller than those of the electronic damage shown in Fig. 4.

Supp. info. 2

The device structure used in the heat transfer simulations is reported in Tab. S3. Compared to the dose simulations and nominal device structure detailed in Tab. S4, it contains a few modifications to facilitate heat transfer modeling. To simplify the stack structure, we assumed that the perovskite/TiO₂ mesoporous layer has thermal properties equivalent to a 100% perovskite layer. The perovskite has lower thermal conductivity and heat capacity than TiO₂, so this is again a conservative estimation. For lack of thermal property data and for simplicity, we ignored the spiro-MeOTAD hole transport layer in the thermal simulations, which is expected to have negligible effect on the outcome. A 1 mm diameter volume was simulated.

A temperature rise in the absorber near the line source of just several K was seen in simulations up to 5000 s duration (on the time scale to a full XRF map but with all dose delivered at a single spot). After 10 s of illumination (time per point is typically < 1 s experimentally), the bulk of the stack is essentially isothermal at the initial condition with a very small volume heated above the equilibrium value due to the beam as shown in Fig. S5. Heat diffuses in the perovskites ~ 1 μ m in ~ 1 μ s. The width of the line source (< 100 nm FWHM) was seen to be not impactful.

Supp. info. 3

For the evaluation of the interaction volume of the X-ray beam with the solar cell stack, Monte-Carlo simulations have been performed based on the layer stack described in Tab. S4. Hereby, the X-ray beam is considered a 1-dimensional pencil beam hitting the solar cell

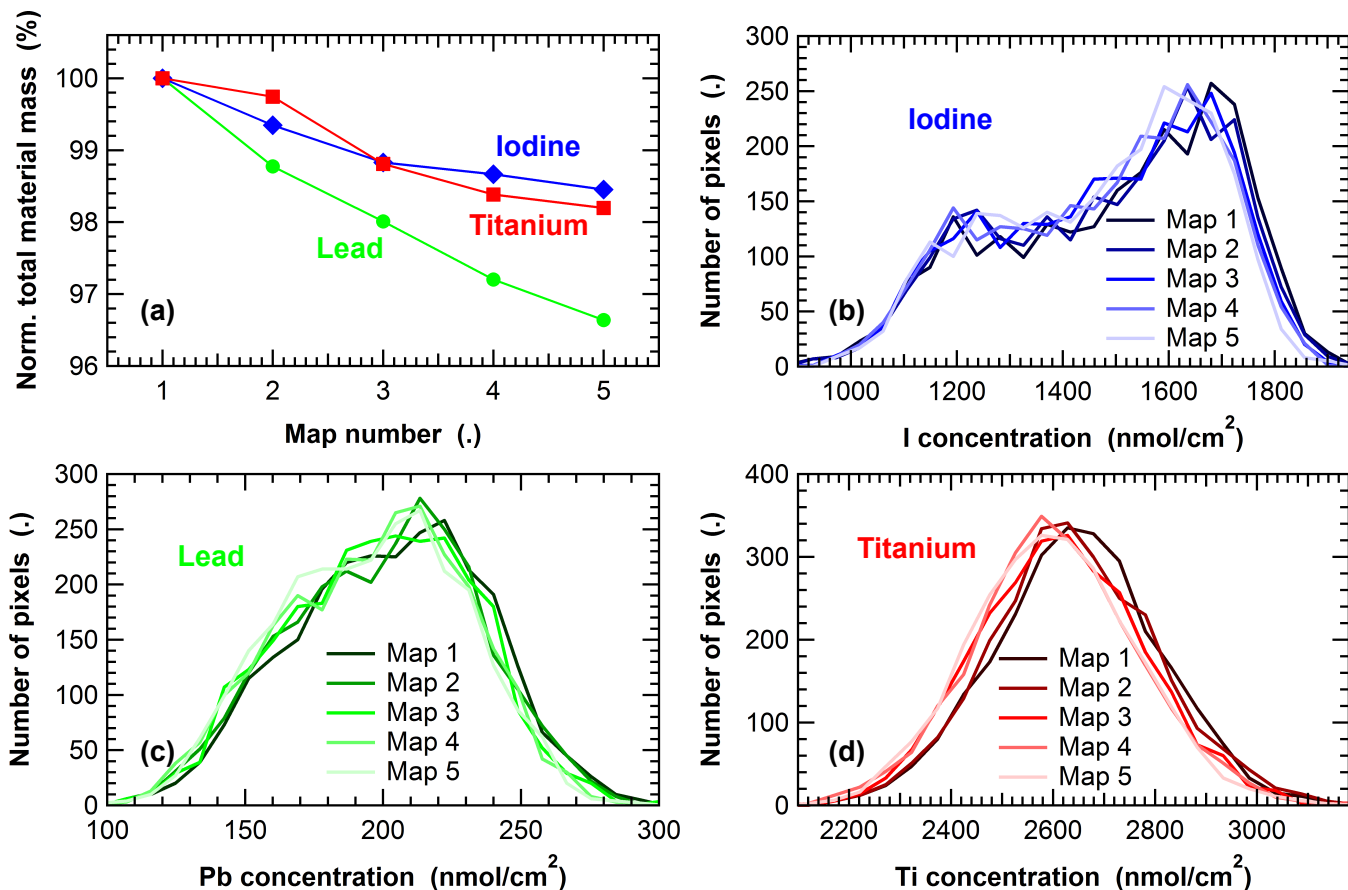


Figure S1: Compositional change during the first 5 measurements shown in Fig. 1. (a): Mass of iodine, titanium, and lead, integrated over the entire maps and normalized to the concentrations of the first map. (b-d): Histograms with the evolution of the elemental concentrations during the 5 measurements.

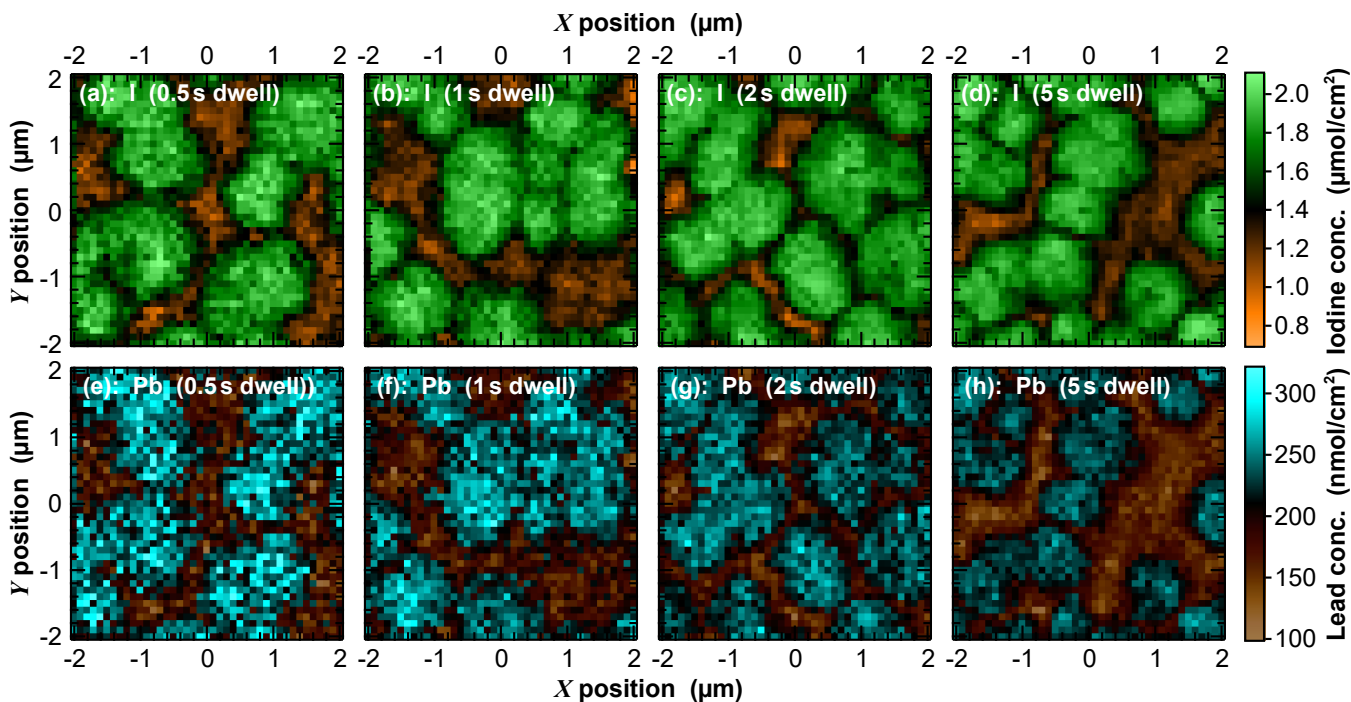


Figure S2: Iodine and lead distribution measured in distinct pristine areas with $100\text{ nm} \times 100\text{ nm}$ pixel size and dwell times from 0.5s to 5s. The color scale is the same for all iodine and lead maps, respectively.

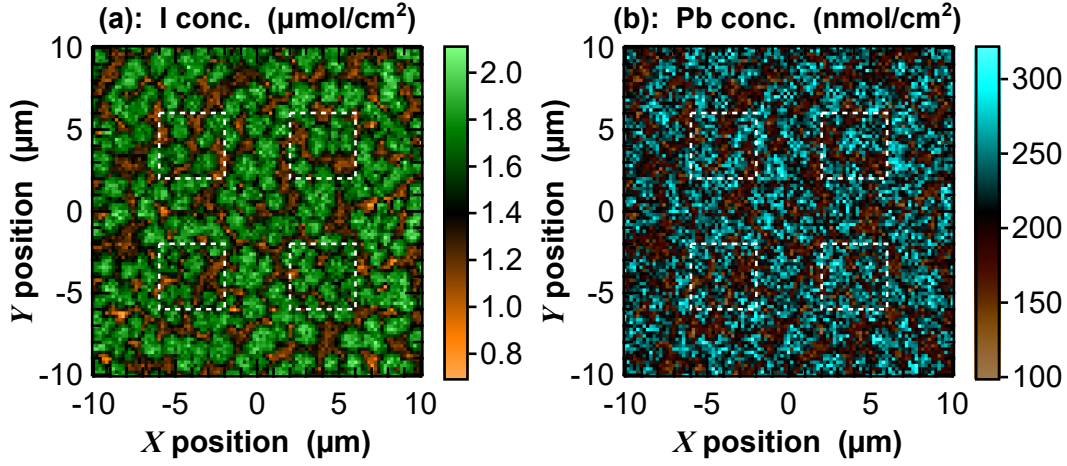


Figure S3: Overview maps showing the iodine and lead distribution after completion of the 4 measurements shown in Fig. S2 whose areas are indicated by white dashed frames. The central positions of these maps are $(X, Y) = (-4 \mu\text{m}, 4 \mu\text{m})$ for Fig. S2(a&e) with 0.5 s dwell time, $(X, Y) = (4 \mu\text{m}, 4 \mu\text{m})$ for Fig. S2(b&f) with 1 s dwell time, $(X, Y) = (4 \mu\text{m}, -4 \mu\text{m})$ for Fig. S2(c&g) with 2 s dwell time, and $(X, Y) = (-4 \mu\text{m}, -4 \mu\text{m})$ for Fig. S2(d&h) with 5 s dwell time. The overview map was taken with $200 \text{ nm} \times 200 \text{ nm}$ pixel size and 0.5 s dwell time, minimizing artifacts from this scan.

Table S1: Fit parameters describing the kinetics of the iodine and lead concentration decrease shown in Fig. S4 that were fitted with $C(t) = C_0 + A \cdot e^{-t/\tau}$. Errors indicate \pm one standard deviation.

Element	X-coord. (μm)	Y-coord. (μm)	C_0 (nmol/cm^2)	A (nmol/cm^2)	τ (s)
Iodine	-0.5	0.5	1228.7 ± 6.1	252.5 ± 7.4	250 ± 20
Iodine	0.5	0.5	800 ± 200	250 ± 200	1750 ± 880
Iodine	0.5	-0.5	1101.6 ± 2.9	357 ± 10	118.0 ± 5.8
Iodine	-0.5	-0.5	1100 ± 70	356 ± 66	940 ± 220
Lead	-0.5	0.5	173.97 ± 0.84	54.1 ± 4.9	66.0 ± 8.2
Lead	0.5	0.5	150 ± 130	-7 ± 130	2300 ± 2200
Lead	0.5	-0.5	179.10 ± 0.92	51.6 ± 4.6	80 ± 10
Lead	-0.5	-0.5	178.0 ± 1.6	33.7 ± 3.1	183 ± 32

Table S2: Fit parameters describing the kinetics of the X-ray beam induced current (XBIC) decrease shown in Fig. 3 for three different X-ray attenuation filters with transmittance T . The measured signal was normalized by the filter transmittance and fitted with $\text{XBIC}(t) = \text{XBIC}_0 + A_1 \cdot e^{-(t-1\text{s})/\tau_1} + A_2 \cdot e^{-(t-1\text{s})/\tau_2}$, which we found to be the simplest model to describe the XBIC decay adequately. Errors indicate \pm one standard deviation.

T %	XBIC_0 (.)	A_1 (.)	τ_1 (s)	A_2 (.)	τ_2 (s)
100	0.50577 ± 0.00051	0.3672 ± 0.0024	11.96 ± 0.14	0.35542 ± 0.00085	198.2 ± 1.2
35.3	0.50025 ± 0.00010	0.5773 ± 0.0046	11.47 ± 0.14	0.2610 ± 0.0010	241.6 ± 3.2
4.4	0.5103 ± 0.0019	0.155 ± 0.017	12.2 ± 2.5	0.6777 ± 0.0091	130.8 ± 2.5

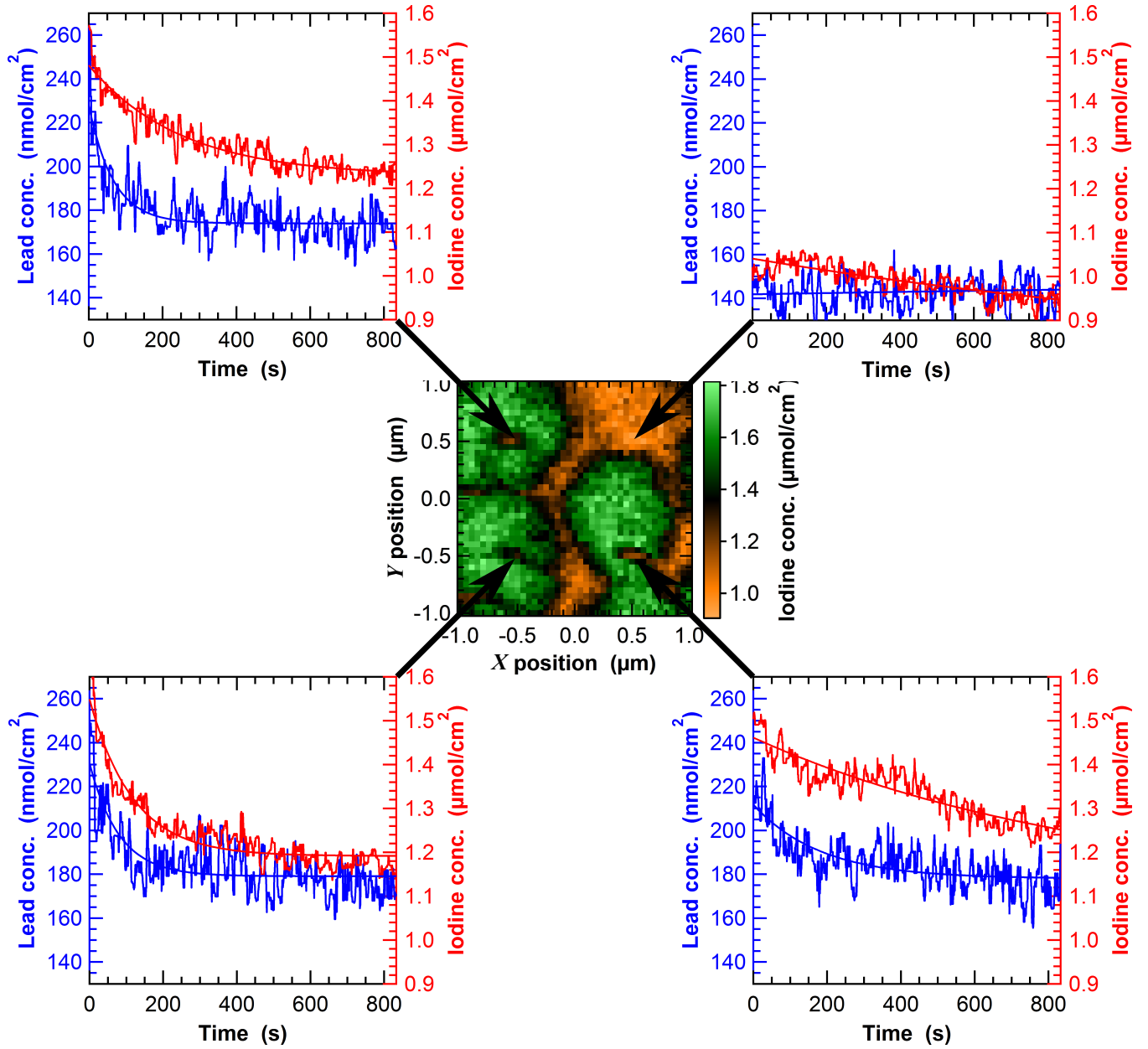


Figure S4: The inner panel displays the iodine distribution recorded after 4 point-wise irradiation sequences at coordinates $(X, Y) = (-0.5 \mu\text{m}, -0.5 \mu\text{m}), (-0.5 \mu\text{m}, 0.5 \mu\text{m}), (0.5 \mu\text{m}, -0.5 \mu\text{m}),$ and $(0.5 \mu\text{m}, 0.5 \mu\text{m})$. The kinetics of the compositional change during the 14-min long irradiation sequences is shown in the outer panels. Lines are fits with exponential functions; the fit constants are given in Tab. S1.

Table S3: Simplified solar cell structure with the parameters used for the thermal heat transfer simulations shown in Fig. S5.

Material	Thickness	Heat capacity	Thermal conductivity	Ref.
Gold	80 nm	0.129 J/(g × K)	317 W/(m × K)	43
CH ₃ NH ₃ PbI ₃	400 nm	183.6 J/(mol × K)	0.75 W/(m × K)	44–46
SnO ₂	300 nm	52.6 J/(mol × K)	25 W/(m × K)	43,47
Glass	100 μm	0.8 J/(g × K)	1.16 W/(m × K)	48

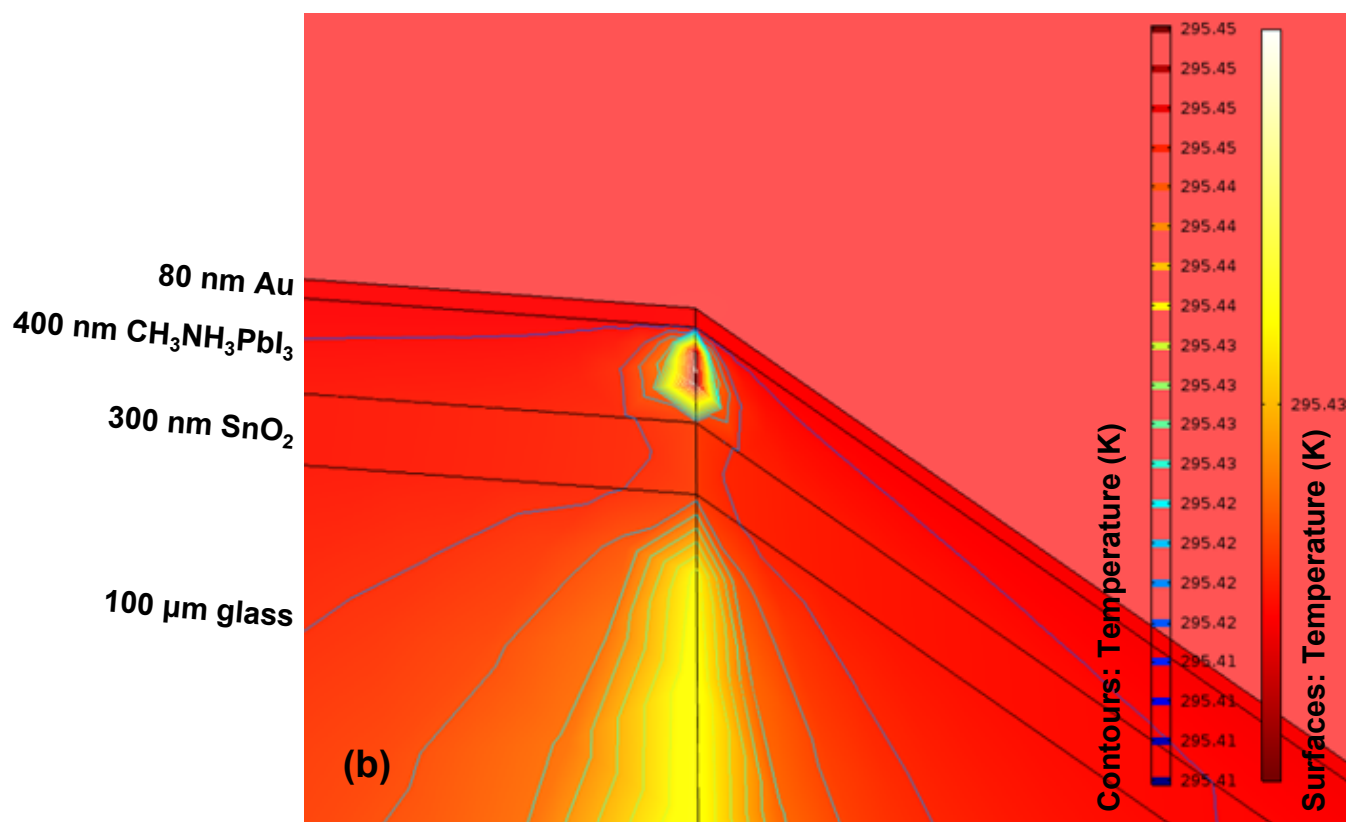
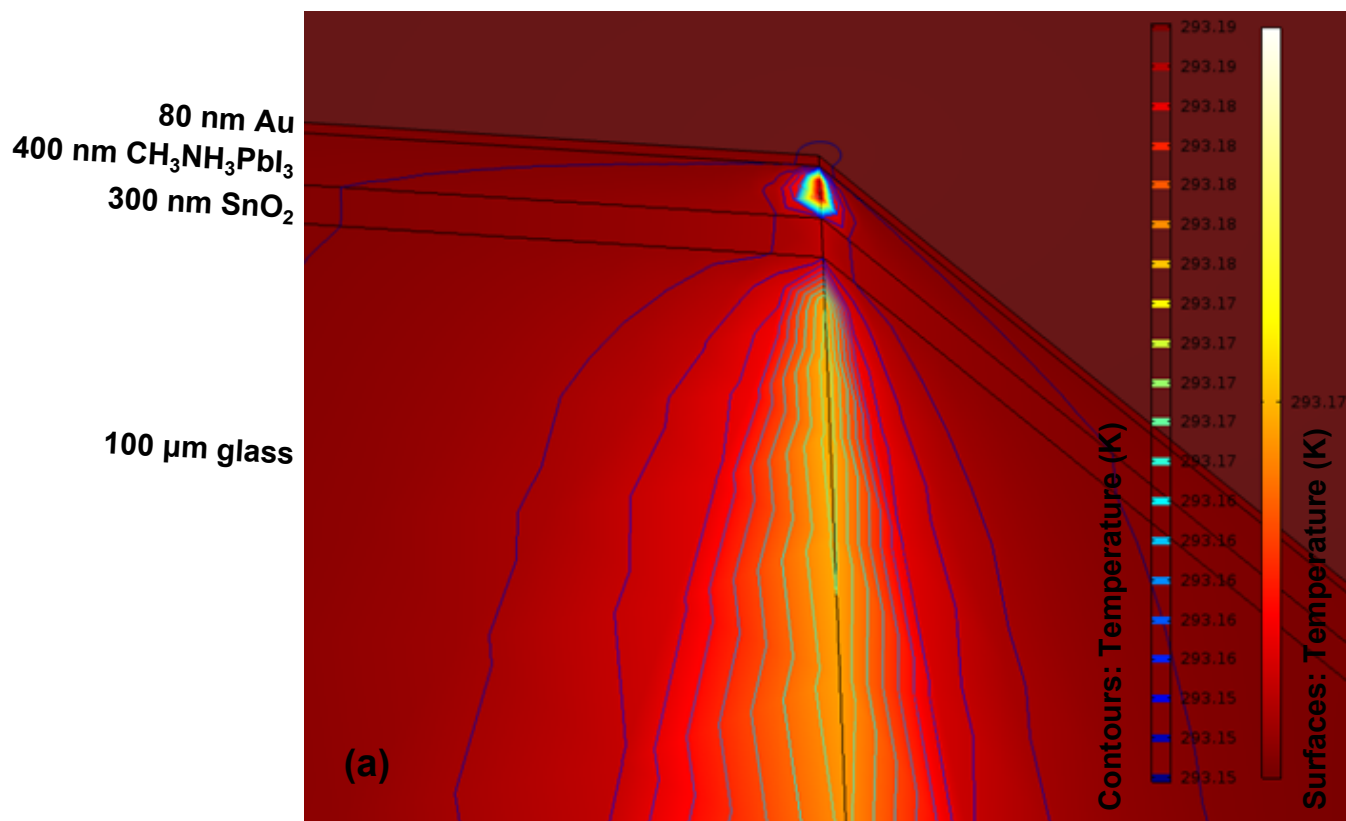


Figure S5: Temperature profile in cross-sections of a simplified sample stack as simulated with the COMSOL Multiphysics® software³³ after 10 μs (upper panel) and 100 s (lower panel) irradiation.

Table S4: Solar cell structure with the layer thickness, density, and elemental composition that served as input for the PENELOPE simulation shown in Fig. S6 & S7.

Material	Thickness (nm)	Density (g/cm ³)	Composition	Ref.
Gold	80	19.3	Au	43
Spiro-MeOTAD	150	1.06	C ₈₁ H ₆₈ N ₄ O ₈	49
Perovskite	80	4	CH ₃ NH ₃ PbI ₃	50
Meso TiO ₂ /perovskite	300	4.09	Ti ₂₆₁₀₅ O ₅₂₂₁₀ C ₃₂₂₆ N ₃₂₂₆ H ₁₉₃₅₅ Pb ₃₂₂₆ I ₉₆₇₈	43
Compact TiO ₂	30	4.17	TiO ₂	43
SnO ₂	300	6.85	SnO ₂	43
Glass	700000	2.43	Si ₂₅₇₅₆ B ₆₃₀₂ Al ₇₈₈₈ Mg ₂₇₂₁ Ca ₁₃₀₄ Sr ₇₅₃ O ₇₇₅₇₅	48,51

stack at $(R, Z) = (0, 0)$ in the coordinate system shown in Fig. S6(a). From this 3D simulation with 10^8 incident photons, we have extracted the dose density, i.e., the energy deposited in the solar cell per unit volume and incident photon as shown as a function of the radial position R and the depth Z . The interaction volume has been quantified based on the dose-density contour area encompassing the volume, within which 68.3% or 95.4% of the total dose has been absorbed. As 100%, the total dose absorbed in the absorber layer was defined. For XBIC, only the dose deposited in the absorber is relevant; there, the $1 - \sigma$ contour encompasses a cylinder with radius $R \approx 100$ nm.

The linear dose density (i.e., the absorbed energy per unit depth and incident photon) is shown in Fig. S6(b). It was calculated as the radially integrated dose density based on the data shown in Fig. S6(a).

The simulations from Fig. S6 have been used to estimate the dose being deposited at a given pixel prior to the XBIC measurement there. Figure S7(a) shows the average 2D dose distribution induced by a single photon in the absorber layer, integrated over the depth Z of the absorber. Figure S7(c) shows the estimation of the effective dose distribution after 1 s of irradiation. It is calculated as the convolution of the single-particle dose distribution from Fig. S7(a) with the 2-D Gaussian shown in Fig. S7(b), representing the idealized beam shape with FWHM $30 \text{ nm} \times 30 \text{ nm}$, and multiplied with the experimentally measured flux (2.6×10^8 photons/s) that was integrated

over 1 s. If the effective dose distribution is shifted by the scan steps and summed over all scanned pixels, the total dose distribution after a scanning microscopy measurement is obtained as shown for a 60×60 pixel scan with $100 \text{ nm} \times 100 \text{ nm}$ pixel size in Fig. S7(d). Figure S7(e) shows a zoom into an edge of Fig. S7(d). This dose distribution corresponds to the situation *after* completion of the entire scan, as seen e.g. by subsequent scans. Due to the symmetry of the dose after the scan completion, all edges show the same pattern with slightly reduced dose towards the edges.

In contrast, Fig. S7(f) shows the dose deposited at a given spot at the time that this precise spot is being measured. In other words, we have evaluated the deposited dose at each pixel *prior* to the intended irradiation of that spot. This corresponds to the situation in a realistic measurement such as in Fig. 2(b), and it is obvious that the first measurement row—and even more the first measured pixel—is evaluated in a more pristine state than subsequent rows and pixels due to the tails of the beam shape that irradiate neighboring pixels far beyond the FWHM of the beam intensity profile.

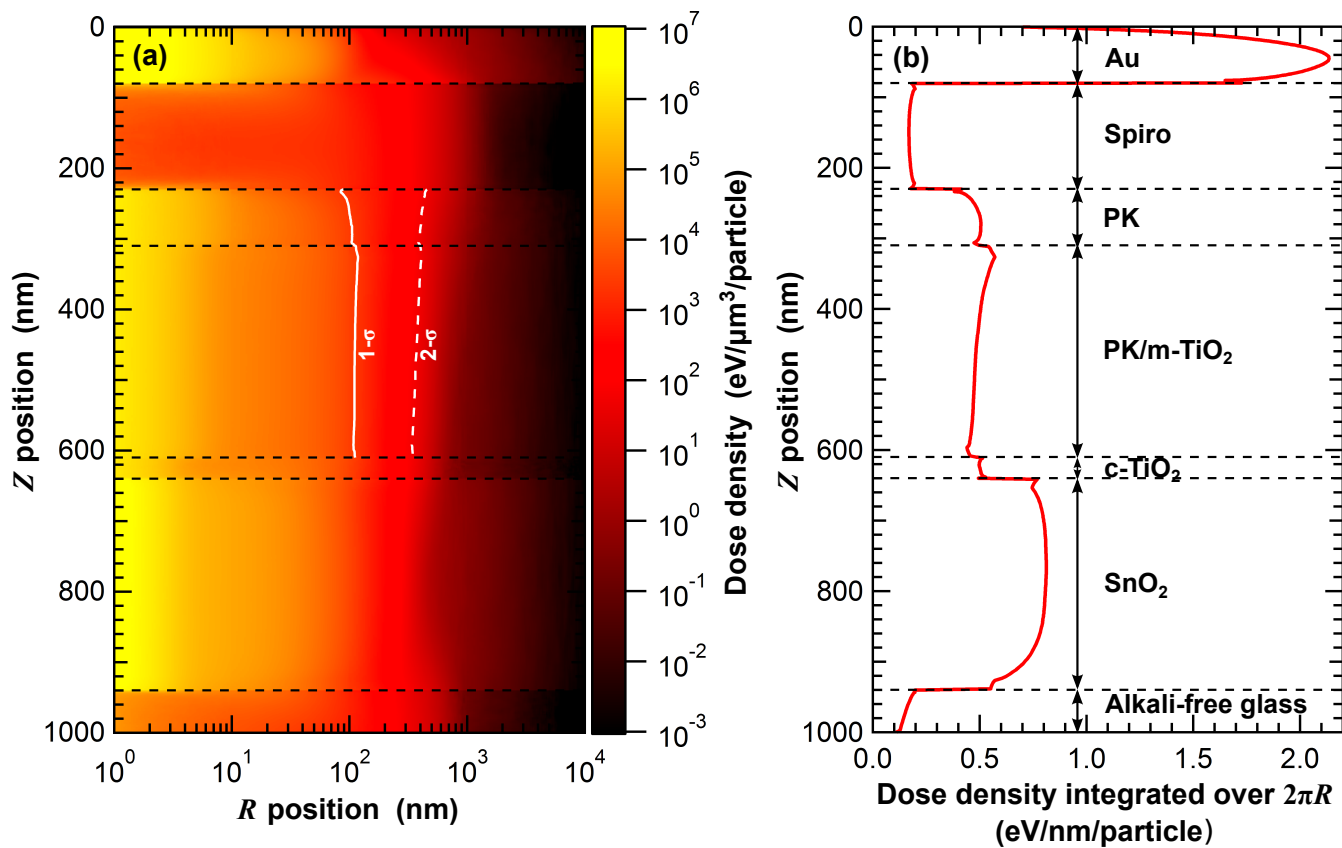


Figure S6: Monte-Carlo based three-dimensional simulation of the dose distribution in a perovskite solar cell for X-ray photons incident perpendicularly at depth $Z = 0$ and radial distance $R = 0$. (a) Radial dose distribution with logarithmic color scale. The white lines indicate the contour areas, at which 68.3% ($1 - \sigma$, continuous line) and 95.4% ($2 - \sigma$, dashed line) of the dose absorbed in the absorber layer is deposited. (b) Radially integrated dose as a function of depth.

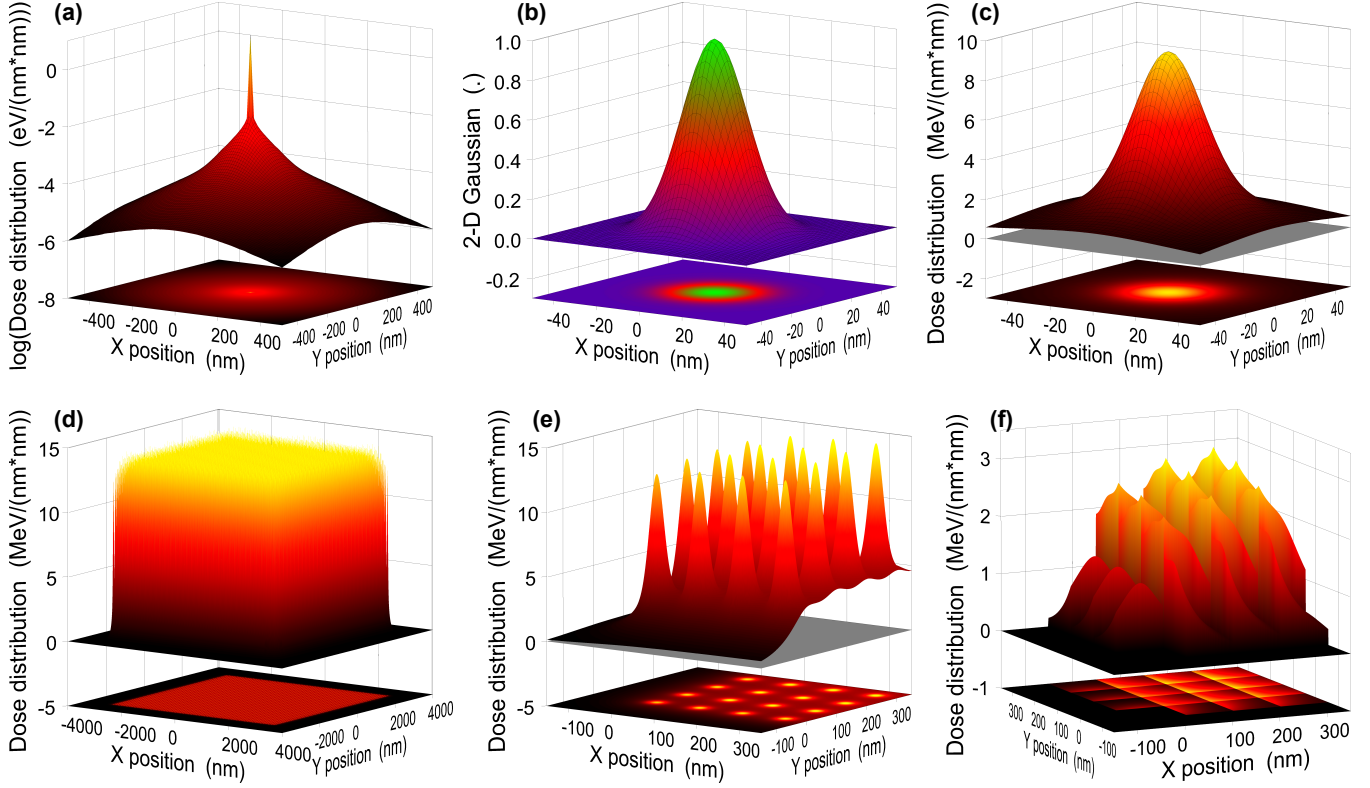


Figure S7: Monte-Carlo based simulation of the dose distribution deposited during XRF/XBIC measurements in the absorber layer of a perovskite solar cell. (a): Average dose distribution caused by a single incident X-ray photon with 9 keV initial energy in the absorber layer of a perovskite solar cell. (b): Gaussian distribution with a FWHM of 30 nm in both X and Y direction, approximating the beam shape of APS beamline 26-ID-C. The function is normalized such that the integrated volume equals 1000 nm^2 . (c): Convolution of the dose distribution from (a) with the Gaussian distribution from (b) and the measured photon flux, integrated over one second. This dose distribution corresponds to the energy absorbed by the absorber within the experimentally used dwell time of 1 s. (d): Convolution of the single-pixel dose distribution from (c) with a scan pattern covering $6 \mu\text{m} \times 6 \mu\text{m}$ with $100 \text{ nm} \times 100 \text{ nm}$ pixel size. This dose distribution corresponds to the absorbed energy after completion of a full scan. (e): Zoom into an edge of (d): due to smaller contributions from neighboring pixels, the edges get less irradiated. (f): Zoom into the dose distribution obtained from the convolution of the single-pixel dose distribution from (c) with the same measurement pattern as in (d), but evaluated prior to the fictive measurement of that pixel, hence corresponding to the dose absorbed at a pixel prior to its evaluation during XBIC measurements.